Strong Correlation of Electrons Studied by Computational Approaches – Physics of Superconductors and Topological Phases

Shiro SAKAI, Takahiro MISAWA, Youhei YAMAJI, Moyuru KURITA and Masatoshi IMADA

Department of Applied Physics, University of Tokyo,
7-3-1, Hongo, Bunkyo-ku, Tokyo 113-8786, Japan

Strong electron correlation is a source of rich and marvelous phenomena, functions and concepts in condensed matter. However, it has hampered reliable treatments by theoretical approaches for a long time and still continues to be a challenge, where the mean-field and single-particle type approximations do not work in many cases. Numerical approaches offer promising tools for this challenge, while the numerical accuracy has to be kept sufficiently high because various orders are severely competing and the systems are often under large quantum fluctuations. Partly thanks to rapid progress in computer power, several numerical methods have been developed for this purpose recently. Here, we focus on the cluster extension of the dynamical mean-field theory (CDMFT) and the multi-variable variational Monte Carlo method (mVMC). The CDMFT has been applied to understanding of the mechanism of the high-temperature superconductivity for the model of the cuprate superconductors, particularly to reveal the origin of the pseudogap phenomena. The CDMFT has made it possible to clarify physics of the anomalous metallic phase of the Hubbard model in two dimensions as relevant to the cuprates. The structure of the pseudogap revealed here as a nodeless gap is essentially important in understanding the superconducting mechanism as well. The mVMC has been applied to understand physics of another family of high-T_c superconductors, iron-based superconductors, where the role of electron correlation effects had been controversial before the studies we review here. A key role of the strong electron correlation has become revealed with the help of supercomputers. The topological phases are the subject of extensive studies for two-dimensional electrons under strong magnetic fields as well as for materials with strong spin-orbit interactions. Recent mVMC calculations revealed an intriguing interplay of the spin-orbit interaction and the electron correlation effect. The possibility of the topological phase purely driven by the electron correlation effect without spin-orbit interactions is another hot subject of the numerical approaches. We here review these numerical studies at frontiers of efforts to understand nature of strongly correlated electrons.

1 Pseudogap in high-T_c cuprates

Despite the intensive studies in the last few decades, high-T_c cuprate superconductors still defy a comprehensive understanding. A key to the superconducting mechanism is in the anomalous “normal state”, from which the superconductivity emerges. In particular, in underdoped cuprates, various experimental probes have observed a gap (pseudogap) behavior in the single-electron excitation spectra as well as in the two-particle responses such as magnetic and transport measurements at temperatures above T_c. Although vast amounts of experimental data have been accumulated to date, the origin of the pseudogap and its relationship to the superconductivity are still controversial.

From a theoretical point of view, the difficulty in studying the cuprates is in the fact that the superconductivity occurs in the carrier-doping region sandwiched by the Mott insulating state and the Fermi liquid state, which are the states of two different limiting cases. The former is a manifestation of the localizing nature of the strongly correlated electrons while the latter manifests the itinerancy of the electrons. This requires a theory for the cuprates to describe the dual character of the electrons simultaneously in a unified fashion. In terms of the quantum field theory, the itinerancy of the electrons is described by the presence of poles of the single-electron Green's function G at the Fermi level; that is, a metal is defined by the presence of the Fermi surface. On the other hand, the locality of the electrons is described by the presence of zeros of G (i.e., poles of the self-energy Σ) at the Fermi level, as it induces a gap in the excitation spectra [1]. Thus the duality of the electrons is translated into the presence of (or proximity to) both poles and zeros in G at low energy.

In order to take into account both poles and zeros at the same time, we need a nonperturbative approach. The cluster dynamical mean-field theory (CDMFT) [2,3] is one of such schemes with a capability to provide information on dynamical properties. It maps in a self-consistent way the original lattice model, like the Hubbard model, onto an effective cluster impurity model comprised of a finite-size interacting cluster and infinite number of noninteracting bath sites. The cluster impurity problem is then solved by an accurate numerical scheme such as the exact diagonalization method and the quantum Monte Carlo (QMC) method. The CDMFT takes into account all the correlation effects within the cluster, so that it can capture in an accurate way the physics caused by short-range electronic correlation effects.

Using the CDMFT, we have explored the two-dimensional Hubbard model in the region of the hole- or electron-doped Mott insulators. At small dopings and at zero temperature, both poles and zeros coexist at the Fermi level, which is a new metallic state of matter. We have shown that its electronic structure indeed accounts for various experimental results found in the anomalous metallic (pseudogap) state of the cuprates (Sec. 1.1). Our result furthermore shows an unprecedented momentum structure of the pseudogap on the positive-energy side, which has been elusive in experiments (Sec. 1.2).

1.1 Pole-zero structure of Green's function

We have first studied the zero-temperature electronic structure underlying the pseudogap state, by applying the CDMFT to the two-dimensional Hubbard model on the square lattice [4,5]. We employed a 2×2 square cluster, and solved the effective cluster impurity problem with the exact diagonalization method. In order to capture the electronic structure in the full momentum space, we took advantage of a truncated Fourier transformation of the cumulant [6], $M = (\omega + \mu - \Sigma)^{-1}$, where ω, μ, Σ are frequency, chemical potential and the self-energy, respectively. Since the cumulant is a well localized quantity in the proximity to the Mott insulator, the Fourier transformation truncated at the cluster size is expected to give a good approximation in that region. This argument was indeed confirmed by our subsequent study on the cluster-size dependence, up to 4×4, with the CDMFT + continuous-time QMC (CTQMC) [7] method [8].

Figure 1 (reproduced from Fig. 2(a) in Ref. 4) shows the electronic structure which we obtained in the region slightly hole-doped to the Mott insulator. Around the middle (red) $G = 0$ surface, spectral function is small because of the large scattering (imaginary part of the self-energy) there. Hence this surface induces a gap behavior in the spectral function, which is identified with the pseudogap found in preceding CDMFT studies [9,10]. Since the $G = 0$ surface crosses the Fermi level around (π, π), its large real part of the self-energy deforms the Fermi surface into a pocket around the nodal point. The presence of the singular surface of the self-energy at the Fermi level indicates that a non-Fermi-liquid ground state underlies the pseudogap phase. The metallic

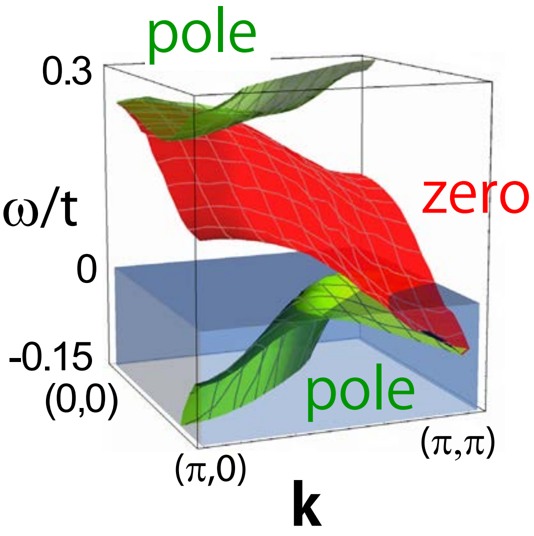

Figure 1: Pole-zero structure of G underlying pseudogap state at temperature $T = 0$ for on-site interaction $U = 8t$ and 9% hole doping to the half filling of two-dimensional Hubbard model, calculated by CDMFT + exact diagonalization method.

state with coexisting pole and zero surfaces also connects the electronic structure of the Mott insulating state at zero doping, where only a zero surface exists around the Fermi level, and the Fermi liquid state at large dopings, where only a pole surface exists.

Furthermore, the spectral function calculated for this pole-zero structure shares many anomalies with what have been experimentally observed in the pseudogap state of the cuprates [5]. The anomalies are attributed to the interference effect between the poles and zeros in the energy-momentum space, that is, the large self-energy around the zero surface deforms and broadens the pole surface into spectra which are out of the standard theory of metals. For example, the Fermi arc [11], back-bending dispersion [12], and the electron-hole asymmetry [13–16] are well reproduced by our CDMFT results.

1.2 *s*-wave pseudogap

Another remarkable feature of the structure in Fig. 1 is that the gap (pseudogap) opens everywhere in the momentum space [4, 5]. This is distinct from the conventionally-assumed *d*-wave structure of the pseudogap. Nevertheless, the calculated spectra are fully consistent with hitherto known ARPES experimental results, as we have mentioned in the previous section, since the gap *below* the Fermi level closes in the nodal direction. Namely, while the gap is around the Fermi level in the antinodal region, it shifts to higher energy as going to the nodal region and eventually locates itself at *above* the Fermi level in the nodal direction. We call this "*s*-wave" pseudogap in the sense that the gap amplitude is finite in the whole momentum space, although the strong momentum dependence of the energy location of the gap discriminates it from the standard *s*-wave gap structure.

Since our *s*-wave pseudogap structure is obtained by an accurate numerical simulation without any assumption on the symmetry or structure of the pseudogap, we took the result seriously and reexamined whether the common belief that the pseudogap is *d*-wave is really founded. In fact, in contrast to the superconducting gap, whose *d*-wave symmetry is firmly evidenced by the SQUID experiments [17, 18], there are no phase-sensitive experimental evidences on the *d*-wave symmetry of the pseudogap. The common belief relies on the ARPES results, which have observed a *d*-wave-like structure of the pseudogap. However, as already discussed above, it cannot be an evidence since only with the occupied spectra observed by ARPES we cannot distinguish the *d*-wave and our *s*-wave pseudogaps. Since the symmetry of the pseudogap is a building block of a number of phenomenological theories, the distinction should play a crucial role in understanding the high-T_c superconductivity.

In order to distinguish the *d*-wave and our *s*-wave pseudogaps in experiments, we need information on the spectra *above* the Fermi level, especially in the nodal region of the momentum space. The momentum structure of the unoccupied spectra has, however, been elusive in experiments. In Ref.19, we explored this dark (unoccupied) side, by combining the electronic Raman spectroscopy experiments and a theoretical analysis based on the cluster dynamical mean-field theory. The advantage of the Raman spectroscopy is that it reflects both the occupied and unoccupied parts of the spectra and has a selectivity of momentum area through exploiting the photon polarizations. In the CDMFT analysis, since a better momentum resolution is required, we employed a 16-site cluster and solved the effective cluster impurity problem with the CTQMC method, which also allows us to study the properties at finite temperatures.

Then we observed the following anomalous behavior in the temperature dependence of the Raman response for underdoped samples. (i) As temperature is lowered from a high temperature, a depression at low frequencies, due to the pseudogap opening, first occurs in the antinodal response. (ii) At a lower temperature, the nodal response begins to decrease in an *intermediate*-frequency region while it increases at around zero energy. These behaviors were indeed well reproduced by our CDMFT Raman calculation, and thereby attributed to the s-wave pseudogap state: (i) is consistent with the fact that the pseudogap in the single-particle spectra opens first in the antinodal region, and (ii) accords with that the pseudogap in the nodal region opens at a lower temperature and above the Fermi level while the quasiparticle peak develops at the Fermi level. The s-wave pseudogap furthermore explains well the electron-hole asymmetry observed in recent ARPES [15, 16] and STM [20] experiments, which would be difficult to be explained within the d-wave pseudogap scenario.

Thus there are mainly two reasons to consider the pseudogap to be the s wave. One is the fact that microscopic numerical simulations, when taking into account all the short-range correlation effects, produce the s-wave structure. The other is the extensive consistency with the experimental observations discussed above. The results impose a strong constraint on our understanding of the pseudogap and of the high-T_c superconducting mechanism in the cuprates.

2 *Ab initio* studies on iron-based superconductors

2.1 Introduction

Iron-based superconductors were discovered in 2008 [21] and the highest critical temperature became above 55 K. It has been shown that most of mother materials of the iron-based superconductors are antiferromagnetic metals [22]. This is in sharp contrast with the other high-T_c superconductors, namely the cuprates, whose mother materials are antiferromagnetic Mott insulators, induced by the strong electron correlation. Thus, at the initial stage of the study, it was not clear whether the electronic correlation is weak or strong in the iron-based superconductors, although it is one of the most important factor to understand the origin of the high-T_c superconductivity.

To clarify the strength of the electronic correlation and its effects on electronic structures such as magnetism and superconductivity in the iron-based superconductors, we applied *ab initio* downfolding scheme [23] to the iron-based superconductors. In this scheme, the global band structures are calculated based on the density functional theory and then the low-energy effective Hamiltonian is obtained by using constrained random phase approximation (cRPA). Finally, we solve the low-energy effective model by employing a high-accuracy low-energy solver such as the multi-variable variational Monte Carlo (mVMC) method and clarify the electronic properties of the target materials in a fully *ab initio* way. In this review, we first explain the basic properties of the low-energy effective model derived for the iron-based superconductors. Then, we will show how the electronic structures of the iron-based superconductors are obtained by solving the low-energy effective models.

2.2 Model

In this report, we consider four iron-based superconductors, namely, LaFePO, LaFeAsO, $BaFe_2As_2$, and FeTe. The obtained low-energy effective model for each iron-based superconductor is a five-orbital Hubbard model and its form is given as

$$\mathcal{H} = \mathcal{H}_0 + \mathcal{H}_{\mathrm{int}} \tag{1}$$

$$\mathcal{H}_0 = \sum_{\sigma} \sum_{i,j} \sum_{\nu,\mu} t_{i,j,\nu,\mu} a^{\dagger}_{i,\nu,\sigma} a_{j,\mu,\sigma} r \tag{2}$$

$$\begin{aligned} \mathcal{H}_{\mathrm{int}} &= \frac{1}{2} \sum_{\sigma,\sigma',i,\nu,\mu} \Big\{ U_{i,i,\mu,\nu} a^{\dagger}_{i,\nu,\sigma} a^{\dagger}_{i,\mu,\sigma'} a_{i,\mu,\sigma'} a_{i\nu,\sigma} \\ &+ J_{i,i,\mu,\nu} \big(a^{\dagger}_{i,\nu,\sigma} a^{\dagger}_{i,\mu,\sigma'} a_{i,\nu,\sigma'} a_{i,\mu,\sigma} \\ &+ a^{\dagger}_{i,\nu,\sigma} a^{\dagger}_{i,\nu,\sigma'} a_{i,\mu,\sigma'} a_{i,\mu,\sigma} \big) \Big\}, \end{aligned} \tag{3}$$

where $a^{\dagger}_{i,\nu,\sigma}$ ($a_{i,\nu,\sigma}$) is a creation (annihilation) operator of an electron with spin σ on the νth maximally localized Wannier orbital at the i-th site. $t_{i,j,\nu,\mu}$ contains single-particle levels and transfer integrals. $U_{i,i,\nu,\mu}$ and $J_{i,i,\nu,\mu}$ are screened Coulomb and exchange interactions, respectively. In the actual calculations, we used the transfer integrals up to the fifth neighbors, which well reproduce the band structures by the local density approximation. Off-site interactions are ignored since those are less than a quarter of the onsite parameters.

The derived effective models are defined in three spatial dimensions at this stage. To explicitly reflect the two-dimensionality of the iron-based superconductors, we performed dimensional downfolding [24] and obtained purely two-dimensional low-energy effective models. Our results of the *ab initio* dimensional downfolding for each compound indicate that the screenings from the other layers reduce all the Coulomb interactions uniformly [24]. Based on our calculated *ab initio* results, we subtract the constant values from $U_{\nu,\mu}$'s in the 3D models [25] as follows; 0.44 eV for LaFePO, 0.41 eV for LeFeAsO, 0.38 eV for $\mathrm{BaFe_2As_2}$, and 0.40 eV for FeTe, respectively. We note that the exchange interactions $J_{\nu,\mu}$ are not significantly changed by the screenings from the other layers [24]. Details of the interaction as well as the single-particle parameters that we used are shown in the literatures [24–27].

From the *ab initio* derivation of the interaction parameters, we have found that family dependence of the interaction parameter can be well scaled by the single parameter λ [25–27], which is defined as $\mathcal{H} = \mathcal{H}_0 + \lambda\mathcal{H}_{\mathrm{int}}$, where $\lambda = 1$ corresponds to the *ab initio* parameters for LaFeAsO. By changing λ, we successfully reproduce the interaction parameters for other materials from those of LaFeAsO. For example, by taking $\lambda \simeq 0.8$, we reproduce the interaction parameters for LaFePO.

2.3 Method

To clarify the electronic structures of the effective models, we employ the mVMC method. Details of the mVMC methods are given in the literature [28]. In the mVMC calculations, we study the ground state properties by employing a generalized Bardeen-Cooper-Schrieffer (BCS) type wave function with the quantum number projection and the Gutzwiller and Jastrow factors;

$$|\psi\rangle = \mathcal{P}_{\mathrm{G}} \mathcal{P}_{\mathrm{J}} \mathcal{L}^{S=0} |\phi_{\mathrm{pair}}\rangle. \tag{4}$$

Here, $\mathcal{L}^{S=0}$ is the spin projection operator to the total spin $S = 0$ subspace; $\mathcal{P}_{\mathrm{G}}$ and $\mathcal{P}_{\mathrm{J}}$ are the Gutzwiller and Jastrow factors, respectively [28]. The spin projection is performed onto the $S = 0$ singlet subspace. The Gutzwiller factor punishes the double occupation of electrons by $\mathcal{P}_{\mathrm{G}} = \exp(-\sum_{i,\nu} g_{i\nu} n_{i\nu\uparrow} n_{i\nu\downarrow})$ where $n_{i\nu\sigma} = a^{\dagger}_{i\nu\sigma} a_{i\nu\sigma}$. The Jastrow factor is introduced up to the next-nearest-neighbor sites as $\mathcal{P}_{\mathrm{J}} = \exp(-\frac{1}{2}\sum_{i,j} v_{ij\nu\mu} n_{i\nu} n_{j\nu})$, where $n_{i\nu} = \sum_{\sigma} n_{i\nu\sigma}$. The one-body part $|\phi_{\mathrm{pair}}\rangle$ is the generalized pairing wave function defined as $|\phi_{\mathrm{pair}}\rangle = (\sum_{\nu,\mu=1}^{5} \sum_{i,j=1}^{N_{\mathrm{s}}} f_{ij\nu\mu} a^{\dagger}_{i\nu\uparrow} a^{\dagger}_{i\mu\downarrow})^{N_e/2}|0\rangle$, where N_e (N_s) is the number of electrons (number of sites). In this study, we restrict the variational parameters, $g_{i\nu}$, $v_{ij\nu\mu}$ to have a 2×1 structure, and $f_{ij\nu\mu}$ to have a 2×2 sublattice structure. The number of variational parameters are 10 for $g_{i\nu}$, 220 for $v_{ij\nu\mu}$, and $100N_s$ for $f_{ij\nu\mu}$. All the variational parameters are simultaneously optimized by using the stochastic reconfiguration method [28, 29]. Our variational wave function $|\psi\rangle$ can flexibly describe superconducting (SC), antiferromagnetic (AF), and paramagnetic (PM) phases as well as their fluctuations on an equal footing. The calculations were done up to 8×8 sites.

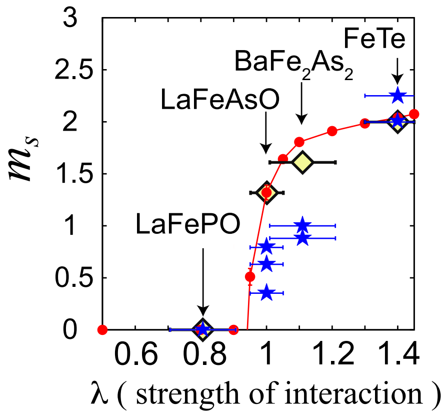

Figure 2: Interaction dependence of magnetic ordered moment m_s [27]. Magnetic ordered moment of each *ab initio* model is represented by (yellow) diamond while experimental magnetic ordered moments for several materials are represented by (blue) stars. By changing the interaction parameter λ for LaFeAsO, we obtain the λ dependence of the magnetic ordered moment [closed (red) circles].

2.4 Results

By using this method, we first clarify that the low-energy effective models can reproduce the family dependence of the magnetic ordered moment m_s [27], which is defined as

$$\boldsymbol{S}_{i\nu} = \frac{1}{2}\sum_{\sigma,\sigma'} a^{\dagger}_{i\nu,\sigma}\boldsymbol{\sigma}_{\sigma\sigma'}a_{i\nu,\sigma'}, \tag{5}$$

$$m(\boldsymbol{q}_{\rm peak})^2 = \frac{4}{3N_s^2}\sum_{i,j,\nu,\mu}\langle \boldsymbol{S}_{i\nu}\cdot\boldsymbol{S}_{j\mu}\rangle, \tag{6}$$

$$m_s = \lim_{N_s\to\infty} m(\boldsymbol{q}_{\rm peak}), \tag{7}$$

where $\boldsymbol{\sigma}$ represents Pauli matrix, $\boldsymbol{q}_{\rm peak}$ is set to $\boldsymbol{q}_{\rm peak} = (0,\pi)$ (stripe magnetic order). As shown in Fig. 2, We calculated the magnetic ordered moment for LaFePO, LaFeAsO, $BaFe_2As_2$, and FeTe and plot them at corresponding λ, which is a measure of the strength of the interaction parameters. The diverse family dependence of the magnetic ordered moment is well explained from the systematic dependence on the strength of the effective electronic interactions. Our calculation also clarifies that LaFeAsO is very close to an antiferromagnetic quantum critical point and this is the origin of the small magnetic ordered moment observed in the experiment.

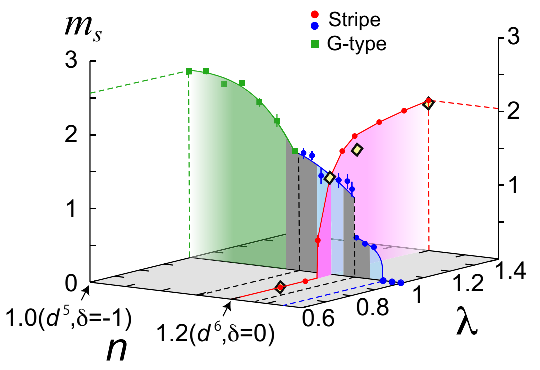

Figure 3: Magnetic ordered moment m_s in the plane of λ and doping concentration δ [27]. The data are plotted in the cross-sections for λ=1 as well as for δ=0. It shows a peak at d^5 (δ=−1.0) and decreases monotonically over d^6 (δ=0), which forms a large half-dome structure peaked at d^5. The mVMC results of the *ab initio* models are shown by (black-framed yellow) diamonds. There exist two first-order transitions (black dashed lines), one indicated by the jumps in the ordered moment around $\delta\sim$0.17 and the other at the transition between the G-type and stripe around $\delta\sim-$0.22, which signals large charge fluctuations under phase-separation effects. In the present short-ranged-interaction model, the phase separation indeed occurs in the gray shaded regions.

In Fig. 3, we show the global phase diagram in the plane of interaction λ and doping concentration δ [27]. Undoped case (six electrons in five orbitals, i.e, d^6 configuration) corresponds to the $n = 1.2$ (red) plane. At $\lambda = 1$, we change the electron density and examine the intrinsic doping effect. By doping electrons, magnetic order vanishes at around 20% doping. In contrast to this, by doping holes, we find unexpected behaviors; magnetic ordered moment becomes larger and larger, and it has a peak at the d^5 configuration. At d^5 configuration, the checkerboard-type (G-type) antiferromagnetic Mott insulator appears. This result indicates that the iron-based superconductors are located on the foot of large dome structures originating from the d^5 Mott insulator.

Here, based on our *ab initio* study, we compare the iron-based superconductors with the other high-T_c superconductors, the cuprates. Both materials are under the proximity effects of the Mott insulator. However, in the iron-based superconductors, due to the multi-orbital effects and the large Hund's rule coupling, the antiferromagnetic dome ranges from d^5 to d^6. This is in sharp contrast with the cuprates, where the proximity effect of the Mott insulator collapses with a small umbrella below 20-30% doping around d^9. In the iron-based superconductors, at the foot of the large d^5 Mott insulator, several intriguing phenomena such as high-T_c superconductivity are found. It is an intriguing issue to reveal the relation between the proximity effects of the d^5 Mott insulator and the high-T_c superconductivity.

3 Correlated Topological Insulators

Emergence of topologically-protected edge states, which are not affected by impurities or imperfection in crystalline electron systems, has been a central issue of quantum Hall insulators realized in two-dimensional electron gases under strong magnetic fields.

Together with pioneering works [30–33], theoretical prediction of quantum *spin* Hall insulators by Kane and Mele [34] has triggered intensive experimental and theoretical studies. Now, the emergence of topologically-protected edge (or surface) states has been recognized as rather universal phenomena: A certain class of insulators, including well-studied polymer polyacetylene and thermoelectric compound $\mathrm{Bi_2Te_3}$, has protected edge/surface states irrespective of their spatial dimensions [35–38].

For essentially non-interacting electron systems, these quantum phases with protected surface states have been classified by using symmetric properties of these systems [36–38].

However, studies on topological states of strongly-correlated electron systems are still ongoing. There are mainly three issues of the studies on topologically non-trivial gapped phases of strongly correlated electron systems:

1. Correlation effects on topological insulators classified in corresponding non-interacting systems.
2. Topological insulators induced by spontaneous symmetry breakings, often called topological Mott insulators.
3. Emergent topological phases of many-body systems that do not appear in non-interacting systems, such as Haldane phases in one-dimensional integer-spin Heisenberg models.

Here, we reiew our numerical study [39] on the first issue in the above list. By using mVMC, we studied a typical model for topologically non-trivial correlated insulators called Hubbard-Kane-Mele model detailed below. The topologically non-trivial phase can in principle be probed by directly calculating the Z_2 topological number. However, it is a formidable computational task. Alternatively and equivalently, the gapless edge probed by the Drude weight concomitant with the gapful bulk state on the cylinder ensures the existence of the topologically nontrivial phase [34]. Our VMC results on the edge Drude weights reveal that the electron correlations enhance spin transports at the edge while charge transports are suppressed. We also give a brief summary of our studies on the second issue.

3.1 Hubbard-Kane-Mele model

We employ a tight binding hamiltonian on the two-dimensional honeycomb lattice proposed by Kane and Mele [34] with inclusion of the spin-orbit coupling as complex hopping terms and the on-site Coulomb interaction, and without the Rashba term to study electron correlation effects on the topological insulator. Hereafter we call this simple model the Hubbard-Kane-Mele model and it is defined as

$$\hat{H} = \hat{H}_{\mathrm{KM}} + U\sum_{I}\hat{n}_{I\uparrow}\hat{n}_{I\downarrow}, \tag{8}$$

with

$$\begin{aligned}\hat{H}_{\mathrm{KM}} &= -t\sum_{\langle I,J\rangle\sigma}\hat{c}^{\dagger}_{I\sigma}\hat{c}_{J\sigma} \\ &+ it_2\sum_{\langle\langle I,J\rangle\rangle\alpha\beta}\nu_{ij}\hat{c}^{\dagger}_{I\alpha}[\sigma_z]_{\alpha\beta}\hat{c}_{J\beta},\end{aligned} \tag{9}$$

where $\hat{H}_{\rm KM}$ is the Kane-Mele hamiltonian, t (t_2) is the nearest-neighbor (next-nearest-neighbor) hopping, and U is the onsite Hubbard interaction. Here we define $\nu_{ij}{=}\vec{d}_i \times \vec{d}_j / \left|\vec{d}_i \times \vec{d}_j\right|$, and $I{=}(i,a)$ ($a{=}A,B$) (see Fig.4(a)).

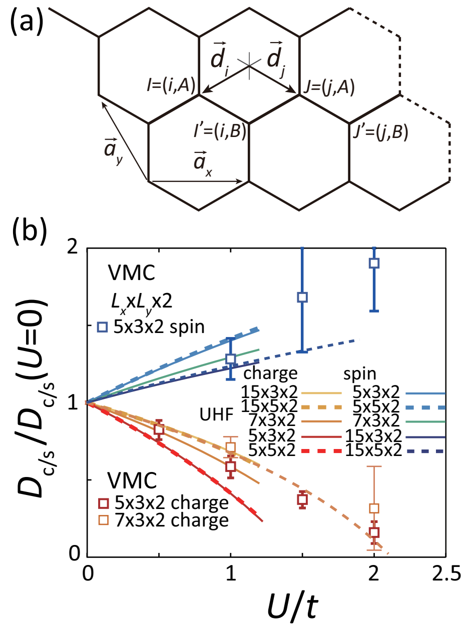

Figure 4: (a) Honeycomb lattice on which the Hubbard-Kane-Mele model is defined. (b) U dependence of charge and spin Drude weights renormalized with the Drude weight for $U = 0$. For comparison, we also show the results of a partially unrestricted Hartree-Fock approximation with prohibition of x and/or y components of spin densities, denoted as UHF in the figure.

To carry out VMC calculations of the Hubbard-Kane-Mele model, we employ a variational wave function defined as

$$|\psi\rangle = \mathcal{P}_{\rm G}\mathcal{P}_{\rm J}|\phi_{\rm pair}\rangle, \tag{10}$$

where $\mathcal{P}_{\rm G}$ and $\mathcal{P}_{\rm J}$ are the Gutzwiller and Jastrow factor, respectively. We impose the Gutzwiller factor on all the sites, whereas introduce the Jastrow factor only along the zigzag edges. The one-body part $|\phi_{\rm pair}\rangle$ is a generalized pairing wave function $|\phi_{\rm pair}\rangle = \left[\sum_{i,j=1}^{N_{\rm s}} f_{ij} c_{i\uparrow}^{\dagger} c_{j\downarrow}^{\dagger}\right]^{N/2} |0\rangle$ with f_{ij} being the complex variational parameters. In this study, we allow f_{ij} to have 2-sublattice ($2 \times L_y$-sublattice) structure or equivalently we have $2 \times 2 \times N_{\rm s}$ ($2 \times L_y \times 2 \times L_y \times L_x$) variational parameters for the torus (cylinder). All the variational parameters are simultaneously optimized by using the stochastic reconfiguration method generalized for complex variables.

3.2 Charge and Spin Drude Weights

Charge and spin Drude weights are calculated by introducing vector potentials as the Peierls factors,

$$t_{IJ\sigma} \to t_{IJ\sigma} \exp[i\vec{A}_{\sigma} \cdot \vec{r}_{IJ}], \tag{11}$$

where $\vec{r}_I = n_I \vec{a}_x + m_I \vec{a}_y$ and $\vec{r}_{IJ} = \vec{r}_I - \vec{r}_J$. Here n_I and m_J are integers, and lattice vectors are $\vec{a}_x$ and $\vec{a}_y$ (see Fig.4(a)). By introducing these Peierls factors, the Drude weights for the charge and spin channels, $D_{\rm c}$ and $D_{\rm s}$, respectively, are calculated from the energy stiffness

$$D_{\rm c} = \frac{1}{2}\frac{d^2 E(\vec{A}_{\uparrow}, \vec{A}_{\downarrow})}{d|\vec{A}|^2}\Bigg|_{\vec{A}_{\uparrow}=\vec{A}_{\downarrow}=|\vec{A}|}, \tag{12}$$

and

$$D_{\rm s} = \frac{1}{2}\frac{d^2 E(\vec{A}_{\uparrow}, \vec{A}_{\downarrow})}{d|\vec{A}|^2}\Bigg|_{\vec{A}_{\uparrow}=-\vec{A}_{\downarrow}=|\vec{A}|}, \tag{13}$$

where $E = \langle\psi|\hat{\mathcal{H}}|\psi\rangle / \langle\psi|\psi\rangle$ is the total energy. If we introduce spin-dependent vector potentials, $\vec{A}_{\sigma}{=}\sigma\vec{A}$, we obtain the Drude weight for the spin channel, namely the spin Drude weight. To clarify the edge state, we employ a cylinder with sizes $N_s{=}L_x{\times}L_y{\times}2$, for the honeycomb lattice with two sites on a unit cell and the periodic (free) boundary conditions in the x (y) directions. We have confirmed that the employed width L_y is large enough to make isolated two edges at the two free boundaries at $y = 0$ and $y = L_y$. For the bulk properties we employ the torus, where the boundary is periodic for all the directions .

We show our VMC results for the Drude weights for the Hubbard-Kane-Mele model on the cylindrical geometry with two zigzag edges along the x-direction in Fig.4(b). The electron correlations enhance the spin Drude weight $D_{\rm s}$

of the edge states while the electron correlations suppress the charge Drude weight D_c. In other words, the electron-electron interactions induce localization of the charge degrees of freedom and enhance the spin conduction. Our results suggest that pure spin conductions are induced by the electron correlation at the edge/surface of the topological insulators.

3.3 Topological Mott insulator

Both in two and three dimensions, the topological insulators are typically realized in the presence of strong spin-orbit interaction [40–42]. On the other hand, it was suggested that the extended Hubbard model on the honeycomb lattice can generate an effective spin-orbit interaction from a spontaneous symmetry breaking at the Hartree-Fock mean-field level and results in the topologically non-trivial phase [43]. Similar phenomenon has also been proposed on the kagomé, diamond and pyrochlore lattices [44–46]. A common property is that the lattice models which are semimetals in the single particle problem may have topologically nontrivial insulator phases caused by the Coulomb interaction. Therefore, these states are called topological Mott insulators. These proposals offer the possibility of the realization of the topological insulator even in the absence of the spin-orbit interaction.

Theories of the topological Mott insulators also opens a possibility of studying quantum phase transitions with novel criticality [47]. Contrary to the ordinary phase transitions, where the universality class is determined by spatial dimension and the structure of broken symmetries, criticality of the transition to the topological Mott insulator depends on the band dispersion near the Fermi point characteristic of the zero-gap semiconductors. In the topological Mott insulators, the criticality of the system is calculated from a free energy expansion

$$f[\zeta] - f[0] \simeq AQ + BV\zeta^2, \tag{14}$$

$$Q = \int_0^\Lambda k^{d-1} dk \left[-\sqrt{aV^2\zeta^2 + bk^{2n}} + bk^n \right]. \tag{15}$$

Here, A, B, a, b are constants depending on the system, V is the control parameter, ζ is the order parameter, Λ is the cut-off wave length, d is the spatial dimension of the system, and n is the exponent which determines the band dispersion near the Fermi point. Therefore, the topological change of the Fermi surface leads to a free-energy singularity $|\zeta|^{d/n+1}$, and generates unconventional universalities characterized by mean-field critical exponents $\beta = n/(d-n)$ and $\delta = d/n$.

For more quantitative estimate of the critical exponents by considering fluctuations, for example, fermionic renormalization group [48] or a renormalization group method applicable to non-analytic free-energy expansions, which may give a modification to our analysis, will be helpful and are left for future studies. These may give a solution for dynamical exponents and upper critical dimensions of the topological Mott transition, and hence give the estimate for quantitative corrections of the other critical exponents as well. Furthermore, strong quantum fluctuations expected around the present topological Mott transition may offer a basis for unprecedented quantum phases mediated by the spin-orbitons.

References

[1] I. Dzyaloshinskii: Phys. Rev. B **68** (2003) 085113.

[2] G. Kotliar, S. Y. Savrasov, G. Palsson, and G. Biroli: Phys. Rev. Lett. **87** (2001) 186401.

[3] T. Maier, M. Jarrell, T. Pruschke, and M. H. Hettler: Rev. Mod. Phys. **77** (2005) 1027.

[4] S. Sakai, Y. Motome, and M. Imada: Phys. Rev. Lett. **102** (2009) 056404.

[5] S. Sakai, Y. Motome, and M. Imada: Phys. Rev. B **82** (2010) 134505

[6] T. D. Stanescu and G. Kotliar: Phys. Rev. B **74** (2006) 125110.

[7] E. Gull *et al.*: Rev. Mod. Phys. **83** (2011) 349. .

[8] S. Sakai *et al.*: Phys. Rev. B **85** (2012) 035102.

[9] B. Kyung, S. S. Kancharla, D. Seńećhal, A.-M. S. Tremblay,M. Civelli, and G. Kotliar: Phys. Rev. B **73** (2006) 165114.

[10] A. Macridin, M. Jarrell, T. Maier, P. R. C. Kent, and E. D'Azevedo: Phys. Rev. Lett **97** (2006) 036401.

[11] M. R. Norman, H. Ding, M. Randeria, J. C. Campuzano, T. Yokoya, T. Takeuchi, T. Takahashi, T. Mochiku, K. Kadowaki, P. Guptasarma, and D. G. Hinks, Nature **392** (1998) 157.

[12] A. Kanigel, U. Chatterjee, M. Randeria, M. R. Norman, G. Koren, K. Kadowaki, and J. C. Campuzano: Phys. Rev. Lett. **101** (2008) 137002.

[13] T. Hanaguri, C. Lupien. Y. Kohsaka, D.-H. Lee, M. Azuma, M. Takano, H.Takagi, and J. C. Davis: Nature **430** (2004) 1001.

[14] P. W. Anderson and N. P. Ong: J. Phys. Chem. Sol. **67** (2006) 1.

[15] H.-B. Yang *et al.*: Nature **456** (2008) 77.

[16] M. Hashimoto *et al.*: Nature Phys. **6** (2010) 414.

[17] D. A. Wollman, D. J. Van Harlingen, W. C. Lee, D. M. Ginsberg, and A. J. Leggett: Phys. Rev. Lett. **71** (1993) 2134.

[18] C. C. Tsuei *et al.*: Nature **387** (1997) 481.

[19] S. Sakai *et al.*: Phys. Rev. Lett. **111** (2013) 107001.

[20] A. Pushp *et al.*: Science **324** (2009) 1689.

[21] Y. Kamihara, T. Watanabe, M. Hirano, and H. Hosono: J. Am. Chem. Soc. **130** (2008) 3296.

[22] G. R. Stewart: Rev. Mod. Phys. **83** (2011) 1589.

[23] For a review, see T. Miyake and M. Imada: J. Phys. Soc. Jpn. **79** (2010) 112001.

[24] K. Nakamura, Y. Yoshimoto, Y. Nohara, and M. Imada: J. Phys. Soc. Jpn. **79** (2010) 123708.

[25] T. Miyake, K. Nakamura, R. Arita, and M. Imada: J. Phys. Soc. Jpn. **79** (2010) 044705.

[26] T. Misawa, K. Nakamura, and M. Imada: J. Phys. Soc. Jpn. **80** (2011) 023704.

[27] T. Misawa, K. Nakamura, and M. Imada: Phys. Rev. Lett. **108** (2012) 177007.

[28] D. Tahara and M. Imada: J. Phys. Soc. Jpn. **77** (2008) 114701.

[29] S. Sorella: Phys. Rev. B **64** (2001) 024512.

[30] B. A. Volkov and O. A. Pankratov : JETP Lett. **42** (1985) 178.

[31] O. A. Pankratov, S. V. Pakhomov, and B. A. Volkov : Solid State Comm. **61** (1986) 93.

[32] E. Fradkin, E. Dagotto, and D. Boyanovsky : Phys. Rev. Lett. **57** (1986) 2967.

[33] F. D. M. Haldane, : Phys. Rev. Lett. **61** (1988) 2015.

[34] C. L. Kane and E. J. Mele : Phys. Rev. Lett. **95** (2005) 146802.

[35] L. Fu, C. L. Kane, and E. J. Mele : Phys. Rev. Lett. **98** (2007) 106803.

[36] A. Kitaev, in Proceedings of the L. D. Landau Memorial Conference "Advances in Theoretical Physics",e-print arXiv:0901.2686.

[37] S. Ryu, A. P. Schnyder, A. Furusaki, and A. W. W. Ludwig : New. J. Phys. **12** (2010) 065010.

[38] X.-G. Wen : Phys. Rev. B **85** (2012) 085103.

[39] Y. Yamaji and M. Imada : Phys. Rev. B **83** (2011) 205122.

[40] B. Andrei Bernevig, Taylor L. Hughes, and S.-C. Zhang: Science **314** (2006) 1757.

[41] M. König, S. Wiedmann, C. Brüne, A. Roth, H. Buhmann, L. W. Molenkamp, X.-L. Qi, and S.-C. Zhang: Science **318** (2007) 766.

[42] D. Hsieh, D. Qian, L. Wray, Y. Xia, Y. S. Hor, R. J. Cava, M. Z. Hasan: Nature **452** (2008) 970.

[43] S. Raghu, X.-L. Qi, C. Honerkamp, and S.-C. Zhang: Phys. Rev. Lett. **100** (2008) 156401.

[44] J. Wen, A. Rüegg, C.-C. J. Wang, and G. A. Fiete: Phys. Rev. B **82** (2010) 075125.

[45] Y. Zhang, Y. Ran, and A. Vishwanath: Phys. Rev. B **79** (2009) 245331.

[46] M. Kurita, Y. Yamaji and M. Imada: J. Phys. Soc. Jpn. **80** (2011) 044708.

[47] M. Kurita, Y. Yamaji and M. Imada: Phys. Rev. B **88** (2013) 115143.

[48] I. F. Herbut, V. Juricic, and O. Vafek, Phys. Rev. B **80** (2009) 075432.